Chapter 4

AGB mass loss and stellar variability

In this chapter the relations between the mid-IR emission and pulsation properties of O-rich AGB stars with known long period variability type are studied. The analysis is made by using the tools developed in the previous chapter, and by modeling the sources with steady state spherically symmetric radiative transfer. By fitting the IRAS Low Resolution Spectra of the circumstellar envelopes around each star, the thermal structure, optical depth and mass loss rate are derived. The best fit parameters are then correlated with the central source variability type.

This work has been made in collaboration with Željko Ivezić, Princeton University, and has been presented at the International Workshop "The changes in Abundances in Asymptotic Giant Branch Stars", held in Rome, September 16–18, 1999 (Marengo et al., 2000b). [Results of this analysis finally published on Marengo et al. (2001)]

4.1 Long Period Variability in the AGB phase

On August 3, 1596, David Fabricius, an amateur astronomer native of Friesland (The Netherlands) started a series of observations, aimed to determine the position of a planet which he believed to be Mercury (it was, in fact, Jupiter). He used as reference point a nearby unidentified star of magnitude 3 which, surprisingly, by August 21 had already increased to magnitude 2. When the star faded and finally disappeared in October, Fabricius assumed he had just observed a nova, and then forgot about it. On February 15, 1609, he observed the star reappear, which was quite unusual. Fabricius,

who was a minister, unfortunately did not live to enjoy the appreciation of its discovery, being murdered by a peasant whom he accused from the pulpit of having stolen one of the minister's geese.[1]

The mysterious star was then forgotten, until Johann Fokkens, also of Friesland, saw it again in 1638, determining that it was a variable star with a period of 11 months. The star was finally named *Mira*, which means "The Wonderful" by Johann Hevelius of Danzig, and *o* (omicron) Ceti by Johann Bayer in 1603.

Today, Mira is taken as the prototype for a whole class of variable stars, with periods that can be as long as several hundred days, and whose light curves can be of several magnitudes in the optical. Mira, as other *Long Period Variables* (LPV), is an AGB star, characterized by pulsational instabilities in the atmospheric layers. Radial pulsations, with not fully understood dynamics, are responsible for periodic contraction and relaxation of the stellar photosphere, and thus for the variations of the stellar luminosity.

In the inner part of the LPV atmosphere, the passing shocks cause a periodic modulation of the structure; in the upper layers the dissipation of mechanical energy leads to a levitation, i.e. a density enhancement of up to several orders of magnitude, compared to an hydrostatic atmosphere. Both of these effects can influence the formation of molecules and dust grains, and thus the mass loss properties of the star (Höfner, 1999).

If Long Period Variability is in some way one of the ingredients in dust formation processes in AGB stars, some correlation between the infrared properties of LPVs, which are a function of dust production, and the pulsational characteristics, should be expected. This is what this chapter aims to explore.

4.1.1 Types of Long Period Variability

There are four main types of LPVs that are associated with the AGB phase: Miras (of which *o* Ceti is the prototype), Semiregulars of type "a" and "b", and Irregulars of type "Lb". According to the General Catalogue of Variable Stars (GCVS, Kopolov et al. 1998), they are defined as follows:

Mira: long-period variables with characteristic late-type emission spectra (Me, Ce, Se) and light amplitudes from 2.5 to 11 magnitudes in V. Their periodicity is well pronounced, and the periods lie in the range between 80 and 1000 days. Infrared amplitudes are usually less than

[1] see Hoffleit (1996) for an historical account on Mira discovery.

in the visible, and may be less than 2.5 magnitudes; for instance, in the K band they usually do not exceed 0.9 mag.

SRa: Semiregular variables of type a, which are late-type (M, C, S or Me, Ce and Se) giants displaying persistent periodicity and usually small (less than 2.5 magnitudes in V) light amplitude. Amplitudes and light-curves generally vary, and periods are in the range 35–1200 days. Many of these stars differ from Miras only by showing smaller light amplitudes.

SRb: Semiregular late-type (M, C, S or Me, Ce, Se) giants with poorly defined periodicity (mean cycles in the range of 20 to 2300 days), or with alternating intervals of periodic and slow irregular changes, and even with light constancy intervals. Every star of this type may be assigned a certain main period, but the simultaneous presence of two or more periods of light variation is observed.

Lb: Slow irregular variables of late spectral type (K, M, C and S), which shows no evidence of periodicity, or any periodicity present is very poorly defined and appears only occasionally. Lb stars are in general poorly studied, and may in fact belong to the semiregular type (SRb).

The length of the pulsational period, in the SR class, can be related to the evolutionary phase of the pulsators along the AGB. Two independent studies made by Jura & Kleinmann (1992) and Kerschbaum & Hron (1992) arrived at the conclusion that SRs having period $P < 100^d$ are characterized by low mass loss rates ($\dot{M} \sim 10^8$ M$_\odot$ yr^{-1}) and seem to be on the E-AGB phase. Semiregulars with longer periods have instead a higher mass loss, and presumably are in the TP-AGB. This classification is supported by the detection of the s-element Tc in SRs with $P \gtrsim 100^d$ (Little et al., 1987); Tc is otherwise not observed in most SRs with shorter period. Miras, on the other end, appears to be all in the TP-AGB phase.

However, it is clear from the above classification that the subdivision between the various categories is rather thin, and can be easily biased by the quality and frequency of the observations used for the construction of variable light curve.

According to Kerschbaum & Hron (1996), for example, SRa should be considered not as a class by themselves, but as a mixture of "intrinsic" Miras and SRb. Jura & Kleinmann (1992) ignored this subdivision, arguing that, for an infrared selected sample, SRs can all be considered as a single class.

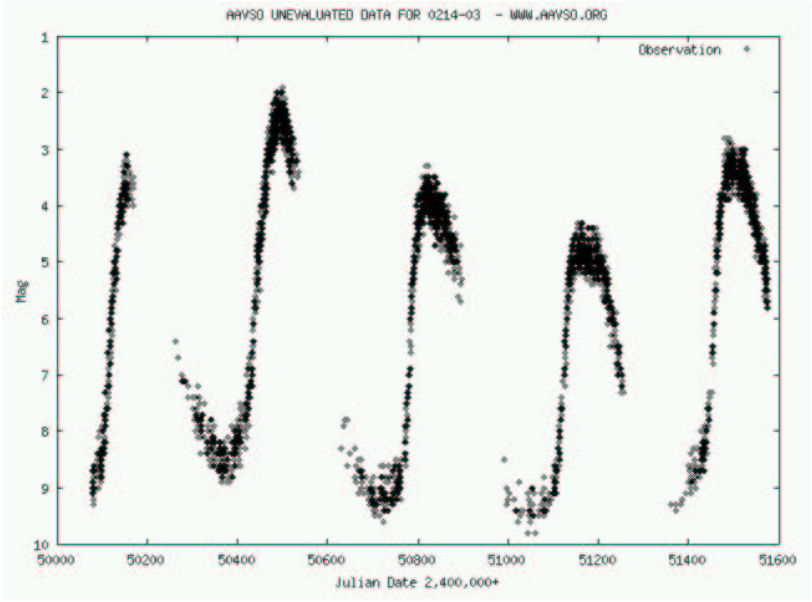

FIG. 4.1.— Light-curve of Mira (o Ceti) during several pulsational cycles. From the American Association of Variable Star Observers (AAVSO) web site (`http://www.aavso.org`).

A cautious approach is thus necessary, to avoid reaching erroneous conclusions by analyzing samples of sources which are in general difficult to define, and can be contaminated by pulsators in a different state.

4.1.2 Pulsation modes in Miras and SRs

An open problem concerning the dynamics of pulsations in Long period Variables is the determination of the pulsational mode. This is somewhat surprising, since the ratio of the fundamental mode and first overtone period in an AGB variable is larger than 2 (Wood & Sebo, 1996). Any reasonable estimate of the radius and mass of an LPV should thus be enough to determine the pulsational mode. This is unfortunately untrue, since a number of observational difficulties can make this measurement rather awkward, and still leave the problem open.

A mass of 1 $M_{\odot}$ is usually adopted in these computations, based on kinematics studies of LPVs in the Galaxy. This value, however, tends to favor first overtone pulsations over fundamental mode, thus biasing the measurement. The determination of the angular radii, also suffers of serious prob-

lems, mainly due to the wavelength dependence of the measured diameters, which requires accurate model atmosphere predictions to be usable. The determination of the distance is also uncertain, even after the HIPPARCOS mission, which provides a large set of reasonable parallaxes. The theoretical models used to analyze the pulsations are also a source of confusion, being not at all clear if classical pulsation theory is applicable to LPVs, or if more refined models are required (Tuchman, 1999).

Fourier analysis of LPV light-curves, can also give direct information on the pulsational mode. An extensive analysis of Mira itself (Barthès & Mattei, 1997) showed a main period of 332.9 days, which is interpreted as first overtone, and a second periodicity of 1503.8 days associated to the fundamental mode. Other analysis of Mira stars made with similar techniques found pulsations which can be interpreted as first overtone pulsation modes. Semiregulars, on the contrary, are often associated to combinations of the first overtone with higher pulsational modes.

Wood et al., (1999), however, by analyzing the relative position in the period luminosity plane of LMC Miras and SRs in the MACHO database, found five distinct period-luminosity sequences. These sequences allowed them to conclude that Miras are *unambiguously* fundamental mode pulsators, while SRs pulsates on a combination of the various overtones.

Even though different analyses are producing contradicting answers, a common result seems to be that SRs appear to pulsate as a combination of higher overtones with respect to Miras. More data and a better understanding of the physics of pulsations in the perturbed atmospheres of variable AGB, are still necessary to provide a reliable answer on this important question.

4.2 A sample of Mira, Semiregular and Irregular variables

In order to test the link between AGB long period variability and mass loss, we have selected a sample of LPVs for which the IRAS mid-IR spectra were available. This sample is characterized in the next section, and then analyzed from the point of view of the mid-IR properties in the LRS spectral region, by studying its mid-IR colors and the shape of the silicate feature.

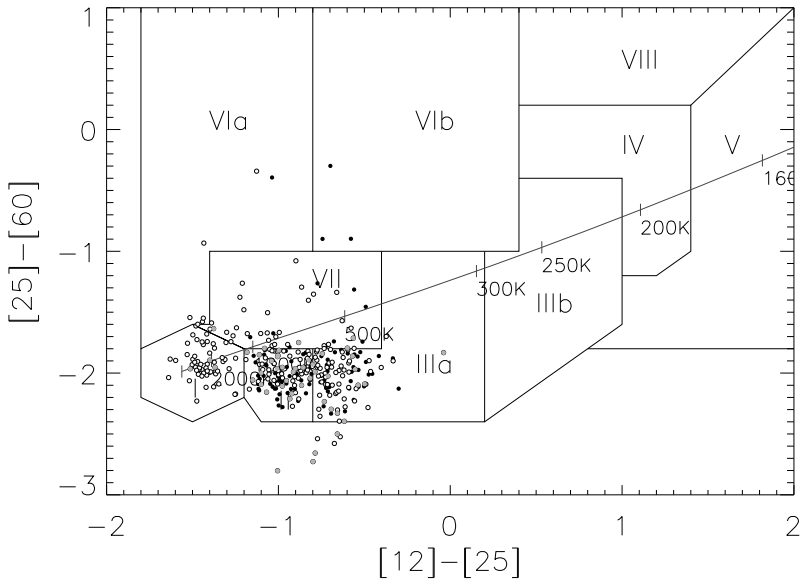

FIG. 4.2.— IRAS [25]-[60] vs. [12]-[25] color color diagram of sources in our KH sample. Miras are filled circle, NMs empty symbols and SRa are grey. The regions are defined according to van der Veen & Habing (1988). The solid line crossing the plot shows the colors of a black body with different temperatures.

4.2.1 Characterization of KH sample

In Ivezić & Knapp (1998) a sample of AGB stars, variable as Mira, SRb and Lb were analyzed in terms of the IRAS [12]-[25] and [12]-K colors. A discrimination was found according to the chemical composition (O-rich vs. C-rich) and the variability type, with SRb and Lb having redder colors than Miras. This evidence was interpreted as a consequence of missing hot dust in the envelopes of SRb and Lb, indicating a recent (order of 100 yr) decrease in the mass loss rate. The sample used in Ivezić & Knapp (1998) was compiled from data published in a series of papers by Kerschbaum, Hron and collaborators (Kerschbaum & Hron, 1996, and references therein), for which the spectral and variability type was known. In this work we have extended the sample in order to include also the stars of type SRa.

We have then limited our analysis to the sources with an O-rich circumstellar chemistry around stars with spectral type M, thus excluding all the S and C stars. This choice was determined by the different optical properties

of O-rich and C-rich dust. The 9.8 μm silicate feature of O-rich envelopes, as shown in section 3.3.3, makes the spectrum of these sources particularly sensitive to small variations of the physical parameters and temperature structures of the envelopes. The almost featureless opacities of amorphous carbon dust present in C-rich envelopes, on the other end, are much less dependent on changes in the dust grain temperature distribution. For this reason, fitting mid-IR spectra (and in particular the inner envelope temperature T_1) is potentially more accurate in the case of oxidic dust.

Of all the sources in the original Kerschbaum & Hron (1996) list, we have excluded also the ones for which the IRAS LRS was unavailable, ending with a list of 432 sources (KH sample, hereafter). In our KH sample 96 are Miras, 48 SRa, 140 SRb and 58 Lb. We have then combined the SRa, SRb and Lb in a single sample of 246 non-Miras (NMs).

To test the possibility that SRa are a spurious class containing a mixture of Mira and SR variables, we have cross correlated the results with a separate sample of SRa sources alone, as a precaution to check if our NMs are "contaminated" by erroneous classified Miras.

The distribution of KH sources in the IRAS color color diagram described in section 3.3.2 is shown in figure 4.2. Note that most of the sources are distributed in regions II and IIIa of the diagram (containing variable stars with young circumstellar envelopes). NMs, however, are also present in region I, where sources without a circumstellar shell (or, rather, having an optically thin one) are located. We have finally cross correlated our sample with the General Catalogue of Variable Stars (GCVS, Kopolov et al. 1998), in order to derive the pulsational period of all sources, when available.

Our sample contains 57 SRs with $P < 100^d$ and 130 with $P \gtrsim 100^d$ which, according to Jura & Kleinmann (1992) and Kerschbaum & Hron (1992) should be in the Early- and TP-AGB phase, respectively. The analyses performed in the following sections are then checked against this subdivision, in order to verify that any eventual difference between Miras and NMs is due to the pulsational mode, and not to the evolutionary status of the sources.

Due to the nature of the samples from which our KH list is derived, and in particular to the limitations in the IRAS catalog, affected by source confusions in the galactic plane, our sample is not statistically complete. Nevertheless, it provides significant indications for the whole class of O-rich galactic AGB variables.

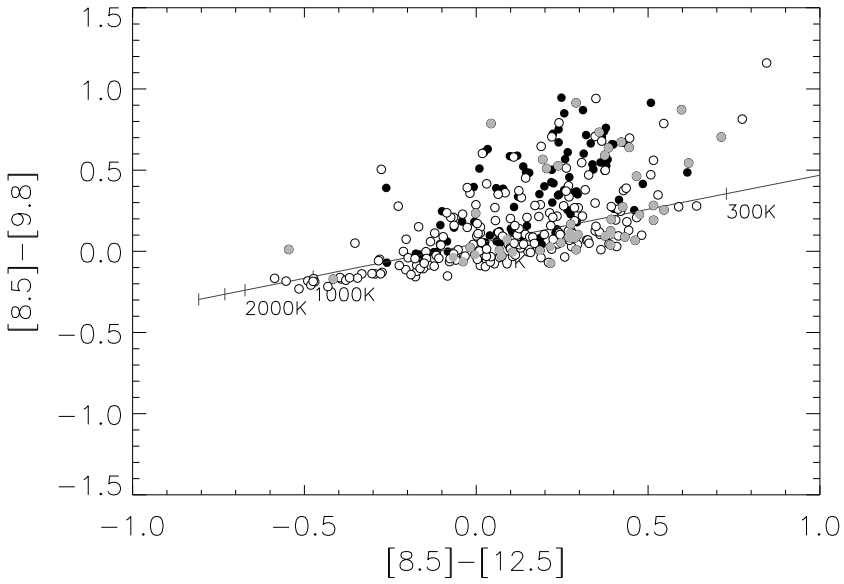

FIG. 4.3.— Silicate color diagram of sources in KH sample. Miras are filled circle, NMs empty symbols and SRa are grey.

4.2.2 Mid-IR colors and variability

Preliminary information on the physical and chemical status of dusty circumstellar envelopes can be obtained by using a suitable photometric system tuned for mid-IR observations, as shown in chapter 3.

As for the test sources used to calibrate our mid-IR color color diagrams, we have derived the photometry in the 8.5, 9.8, 12.5 and 18.0 "standard" gaussian filters by convolving the LRS spectra with the filter profiles, as explained in section 3.3.2. Since all KH sources are O-rich, the "silicate color" diagram is the natural choice to probe the properties of the dust thermal emission in the mid-IR. The plot, shown in figure 4.3, brings into evidence that NMs, and among them most of the SRa, are distributed along the black body line, with a large spread in the [8.5]-[12.5] color. Miras, on the contrary, are clumped above the black body, with $-0.1 \lesssim$ [8.5]-[12.5] $\lesssim 0.5$. This region, as shown in figure 3.10, is mostly populated by envelopes with intermediate optical depth ($1 \lesssim \tau_V \lesssim 30$).

The [8.5]-[9.8] color shows that Miras have a tendency to have a stronger 9.8 μm silicate feature, while NMs and especially SRa tends to be found

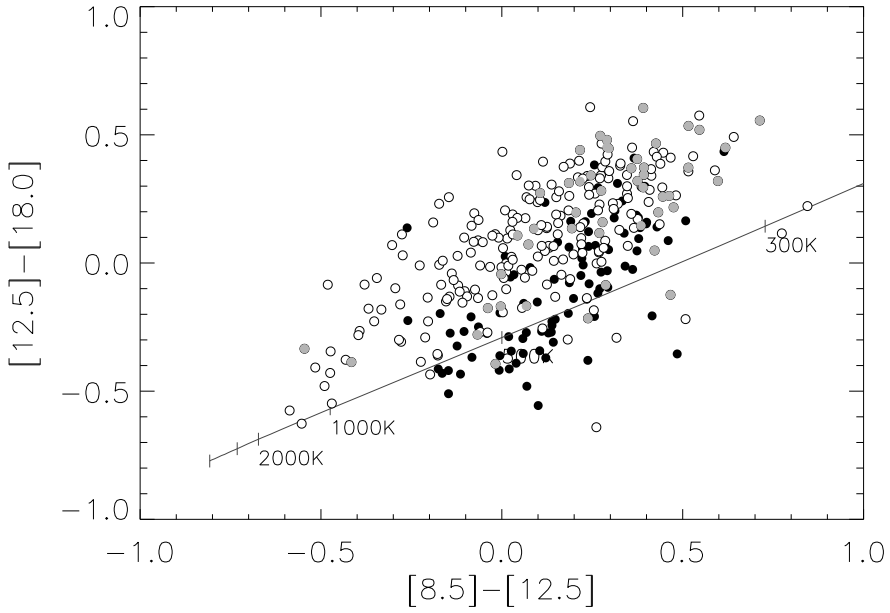

FIG. 4.4.— Dust continuum color diagram of sources in KH sample. Miras are filled circle, NMs empty symbols and SRa are grey.

closer to the black body, where featureless 1n class spectrum are usually located. The absence of a complete separation between Miras and NMs, does not allow to discuss the detailed properties of the silicate feature in the two groups on the basis of the [8.5]-[9.8] color alone. A specific test on the shape of the silicate feature requires the analysis of the full LRS spectra, as described in the next section.

The absence of sources below the black body, in the region otherwise occupied by the 3n class of objects, indicates that the optical depth of KH sources is never high enough to produce a silicate feature self absorbed.

The "thermal continuum" diagram [12.5]-[18.0] vs. [8.5]-[12.5], shown in figure 4.4, does highlight a difference between Miras and NMs, as NMs have an average redder [12.5]-[18.0] color. This cannot be due to a higher optical depth of NM envelopes, which would affect also the "silicate feature" color diagram; it suggests instead the presence of colder circumstellar dust around NMs, as found in Ivezić & Knapp (1998). SRa have a distribution similar to the NMs, but [8.5]-[12.5] $\gtrsim -0.1$ (as for the Miras).

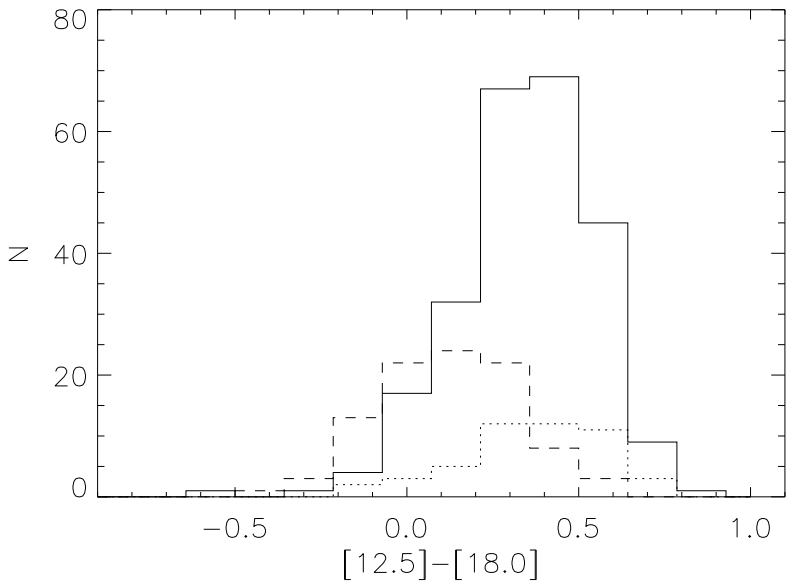

FIG. 4.5.— Distribution of the [12.5]-[18.0] excess colors for Miras (dashed line), NMs (solid line) and SRa (dotted line) for the KH sample.

A quantitative test is provided by the histogram in figure 4.5, and summarized in table 4.1. The histogram plots the distribution of Miras, SRa and NMs in the [12.5]-[18.0] color excess, defined for each source as the difference between its color and the color of a black body with the same [8.5]-[12.5] color temperature. The mean value for this quantity is ~ 0.11 for Miras, ~ 0.32 for NMs and ~ 0.33 for SRa. The 0.2 magnitude difference between the Miras and NMs distribution is larger than the dispersion of the two samples, measured by the variance $\sigma \simeq 0.18$ of both Miras and NMs. We tested this result with a Student's t-test for the mean values, finding that the difference between the two population is indeed statistically significant (see table 4.1 for further details). We then performed the same analysis upon the two SR subsamples with $P < 100^d$ and $P \gtrsim 100^d$, finding a similar color excess in the two cases (0.36 and 0.30 magnitudes), which is not significant with respect to the 0.01 Studen't t-test significance level.

This two tests suggest that, from the point of view of the color temperature of their circumstellar dust, Miras and NMs are two different populations. Among the SR sources, the physical characteristics of the circum-

TABLE 4.1 [12.5]−[18.0] COLOR EXCESS.

Sample	Median [mag]	Mean [mag]	σ [mag]	N sources
Mira	0.10	0.11	0.18	96
NM	0.34	0.32	0.18	246
SRa	0.37	0.33	0.19	48
SR ($P < 100^d$)	0.37	0.36	0.17	57
SR ($P \gtrsim 100^d$)	0.32	0.30	0.20	130

Significance of statistical tests

Sample	F-test	t-test	Result at 0.01 significance[a]
Mira vs. NM	0.90	$6 \cdot 10^{-20}$	Same σ and different mean
SRa vs. Mira	0.70	$2 \cdot 10^{-10}$	Same σ and different mean
SRa vs. NM	0.60	0.71	Same σ and mean
SR $P<100^d$ vs. $P\gtrsim100^d$	0.16	0.05	Same σ and mean

[a] Samples have different σ if the variance F-test returns a significance of 0.01 or smaller, and different mean values if Student's t-test returns a significance of 0.01 or smaller

stellar envelopes are instead homogeneous across all pulsational periods. Assuming the validity of the Kerschbaum & Hron (1992) correlation between pulsational periods and AGB evolution, this is suggestive that SRs form similar circumstellar envelopes in the Early- and TP-AGB phases. The similarity of SRa with NMs, may indicate that there is not a large contamination of Miras in the KH sample.

4.2.3 Variability and the main silicate feature

The shape and characteristics of the 9.8 μm silicate feature observed in the spectra of O-rich AGB circumstellar envelopes is in general affected by many different factors, intrinsic as the grain chemical composition, size distribution, structure (crystalline of amorphous) and degree of processing (e.g. annealing), or extrinsic as the radiative transfer effects due to the envelope optical depth, thermal structure and geometry.

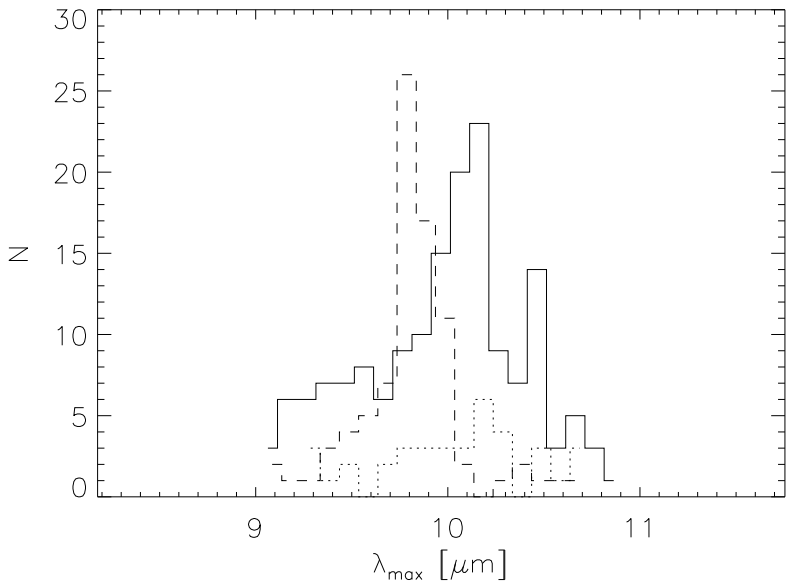

FIG. 4.6.— Distribution of the 10 μm silicate feature peak of KH sources. Dashed line is for Miras distribution, solid line for NMs and dotted line for SRa.

Little-Marenin & Little (1990) first tried to classify a large sample of O-rich AGB variables from the point of view of their silicate feature in the IRAS LRS spectra. They found that their sample of SR and Irregulars was showing a narrower silicate feature, shifted to the red, compared to the Miras. A similar analysis was performed by Hron et al. (1997) with larger statistics, and taking into account the dust continuum emission by fitting it with a separate black body. This later work confirmed the differences between the two classes, finding a shift of about 0.3 μm in the peak position.

In order to probe the KH sources in terms of the shape of their silicate feature, we have fitted each individual IRAS LRS with the best 5 degree polynomial in the 9-11 μm wavelength range. The fitting procedure removes the effect of noise and eventual secondary features, producing "smooth" spectra where the position of the maximum can be easily recognized. The wavelength of the maximum of the best fit polynomial in the given interval is then assumed to be the position of the "true" silicate peak.

With this technique we measured the position of the silicate peak of 85 Miras and 162 NMs; for the remaining sources (11 Miras and 84 NMs) the

Table 4.2 Silicate peak position for KH sources.

Sample	Median [μm]	Mean [μm]	σ [μm]	N sources
Mira	9.87	9.86	0.28	85
NM	10.07	10.01	0.42	162
SRa	10.10	10.08	0.41	37
SR ($P < 100^d$)	10.09	10.04	0.43	31
SR ($P \gtrsim 100^d$)	10.07	10.02	0.38	95

Significance of statistical tests

Sample	F-test	t-test	Result at 0.01 significance[a]
Mira vs. NM	$5 \cdot 10^{-5}$	$5 \cdot 10^{-4}$	Different σ and mean[b]
SRa vs. Mira	$6 \cdot 10^{-3}$	$4 \cdot 10^{-3}$	Different σ and mean[b]
SRa vs. NM	0.82	0.43	Same σ and mean
SR $P<100^d$ vs. $P\gtrsim100^d$	0.41	0.87	Same σ and mean

[a] Samples have different σ if the variance F-test returns a significance of 0.01 or smaller, and different mean values if Student's t-test returns a significance of 0.01 or smaller.
[b] Student's t-test performed in the "unequal variance" case.

fitting procedure failed either because of the excessive noise in the spectrum, or for the absence of a significant feature. Many of the sources for which the silicate feature is too weak are in fact Lb stars of LRS class 1n. Note that the infrared colors of such sources are generally too low (having a color temperature below 1000 K), to identify them as "naked photospheres" (AGB stars without a circumstellar envelope). More probably, they are instead Lb stars with circumstellar envelopes of intermediate optical depth, having the silicate feature partially in self absorption. This is consistent with the distribution of these sources in figure 4.3.

The results are shown in table 4.2, and the histogram with the distribution of λ_{max} is plotted in figure 4.6. We found the mean values for Miras and NMs to be $\langle\lambda_{max}\rangle_{Mira} \simeq 9.86$ μm and $\langle\lambda_{max}\rangle_{NM} \simeq 10.01$ μm respectively, and the median values 9.87 and 10.08 μm. The standard deviation σ_λ is also very different in the two samples, almost twice for NMs (~ 0.42 μm) than for Miras (~ 0.28 μm), indicating a larger dispersion in the silicate feature

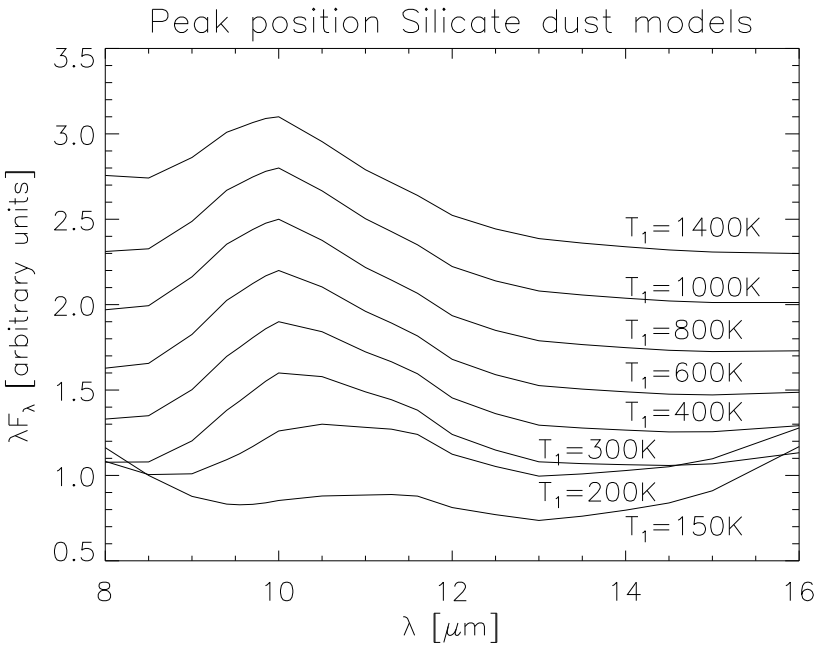

FIG. 4.7.— The position of the 10 μm silicate feature peak for a sequence of models with $\tau_V = 2.9$ and T_1 equal to 1400, 1000, 800, 600, 400, 300, 200 and 150 K.

position for the NMs; this difference is statistically significant with respect to the F-test 0.01 significance level. The Student's t-test for the mean values, performed between the two samples (with unequal variances), confirms the separation of the Mira and NM populations with high significance (0.0005). This result is in agreement with the shift of about 0.2–0.3 μm observed in previous analysis (Hron et al., 1997).

We performed the same test on the SRa class, finding $\langle\lambda_{max}\rangle_{SRa} \simeq 10.08$ μm, and $\sigma_\lambda \simeq 0.41$, very close to the general NM class statistics. This is a further indication that KH SRa do not contain a significant fraction of misclassified Miras. The $\langle\lambda_{max}\rangle$ values for the SR subset with $P \gtrsim 100^d$ and $P < 100^d$ are 10.07 and 10.9 μm respectively, and the σ_λ are 0.43 and 0.39 μm. Again this indicates that the two subclasses are part of the same population.

There are many different reasons that can explain the 0.2 μm shift in the silicate feature position between Miras and NMs. The first possibility is that the composition of dust, and/or oxidation state of the silicate material in the two classes is different, as suggested by various authors (Vardya et al., 1986;

Little-Marenin & Little, 1988; Onaka et al., 1989; Sloan & Price, 1998). A second explanation is that the grain size distribution may be different. This possibility has been explored by Simpson (1991). The results of her work, however, show that to produce a noticeable change in the silicate feature of the envelope spectra, a variation in the dust grain size of at least a factor 7 is required. As argued by Hron et al. (1997), current dynamical models for dust driven winds (Höfner & Dorfi, 1997) indicate that such large variations in the particle size are unlikely to be produced.

There is, however, a third possibility, that is to invoke radiative transfer as the cause of the peak shift. Envelopes with fixed optical depth τ_V and decreasing dust temperature emit an increasing fraction of their thermal radiation at longer wavelengths. This translates in "flat" spectra in which the contribution from the silicate feature, gradually self absorbed, is bound to disappear, until the thermal continuum produces a "bump" in the spectrum which can be interpreted as a shift in the peak of the feature. This effect is shown in figure 4.7 for a sequence of models with $\tau_V \simeq 2.9$ and gradually decreasing dust temperature T_1. Note how the shift becomes very pronounced; this suggests that cold envelopes would have a much larger dispersion in the λ_{max} distribution (as in fact is observed for our NM variables), than envelopes with hotter dust.

4.3 Modeling the mid-IR spectra

To quantify the color temperature difference between KH Miras and NMs, and separate the effects of dust thermal structure and optical depth, we have estimated T_1 and τ_V for each KH source by fitting its LRS spectrum. The adopted best fit procedure is based on χ^2 minimization of the individual spectra with a series of DUSTY models, computed as described in section 3.2. Details on the fitting technique are given in section 4.3.2, and the efficiency in obtaining a good quality fit is discussed in 4.3.3.

As radiative transfer modeling with DUSTY requires to specify the geometry, dust radial density profile and grain size distribution, the dust mass loss rate needed to produce each model envelope is fully characterized by a certain combination of model parameters. The explicit relation between best fit parameters and $\dot{M}_d$ is given in section 4.4, where the statistical distribution of the dust temperature structure and optical depth is also discussed, in terms of the Mira vs. NM dichotomy suggested in the previous sections.

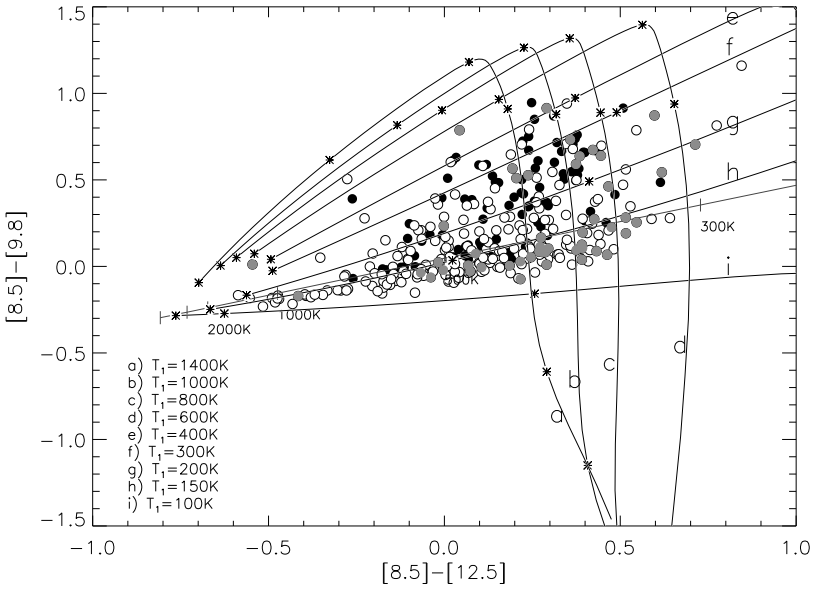

FIG. 4.8.— Silicate color diagram of KH sources with DUSTY models having 2500 K Engelke central source with 10% SiO absorption. Models with T_1 equal to 100, 150, 200, 300, 400, 600, 800, 1000 and 1400 K are plotted.

4.3.1 Model parameter space

Since our KH sample contains only O-rich sources, and has circumstellar envelopes with oxidic dust, we have adopted the full grid of models computed in section 3.2 with the Ossenkopf et al. (1992) dust. The models were run with "standard" MRN grain size distribution, and $n_d(r) \propto r^{-2}$ radial density profile (steady mass loss during the phase in which the current envelope was produced). The inner radius R_1 was fixed by the choice of the inner shell temperature T_1, and the outer envelope radius was scaled as $R_2 \simeq 1000 \cdot R_1$.

As for the brightness energy distribution of the central star, we have tested both the "standard" 2000 K black body, and the Engelke function with 10% SiO absorption described in section 3.2.2. Even though the Engelke + SiO function provides the best fits for dustless sources with "naked photosphere" and envelopes characterized by a very low optical depth, we found that a standard black body is in general a better choice for AGB envelopes with $\tau_V \sim 1$. As shown in figure 4.8 and 4.9: models computed with the Engelke + SiO function have the tendency to produce LRS spectra

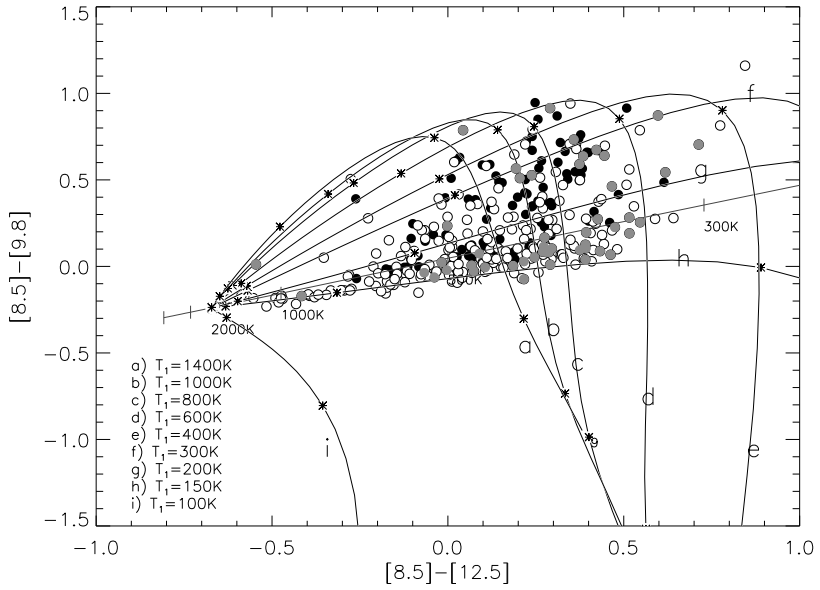

FIG. 4.9.— Silicate color diagram of KH sources with DUSTY models having 2000 K Planck black body central source. Models with T_1 equal to 100, 150, 200, 300, 400, 600, 800, 1000 and 1400 K are plotted.

with an excessive strength of the 10 μm silicate feature (resulting in too high [8.5]-[9.8] color). Models with the black body curve, on the contrary, can better reproduce the distribution of HK sources in the color color plane. For this reason, the analysis which follows has been entirely made using the DUSTY models with Planck black body central source.

A fine logarithmic grid of models with τ_V from 10^{-3} to 231, and T_1 from 100 to 1400 K was used, with 60 steps in τ_V and 31 in T_1, in order to provide the necessary precision in the best fit parameters. Note in figure 4.9 how the coldest dust family of models (track with $T_1 \simeq 100$ K) is totally inadequate to fit any source in the KH sample. The coldest models able to provide a good fitting of the sources, have $T_1 \simeq 150$ K, which can be assumed as a rough estimate of the minimum inner shell temperature in our sample of AGB envelopes.

A subset of models with T_1 restricted to the interval 630–1400 K ("hot dust" models hereafter) was then extracted from the full set, in order to test whether "cold dust" models with lower T_1 are really necessary to improve the fitting of certain classes of spectra.

4.3.2 Fitting technique

The best fit models for each source in our sample were found with a χ^2 minimization routine applied to the source and model spectra in the IRAS LRS wavelength range only. Even though the IRAS point source photometry was available for all sources, and easily derived for the models, we decided to restrict the fitting procedure to the 7–23 μm interval. This decision was made in order to avoid galactic cirrus contamination at longer wavelengths, and the phase dependence of optical and near-IR photometry with the LPV of the sources.

For each source in the sample, the models were individually renormalized to match the absolute flux scale of the source LRS. The normalization factor α of each model was computed by least square minimization of the distance between model and source:

$$\alpha = \frac{\sum_{i=1}^{N} \left(\lambda_i F_\nu^S \cdot \lambda_i F_\nu^M\right)}{\sum_{i=1}^{N} \left(\lambda_i F_\nu^M\right)^2} \tag{4.1}$$

where $\lambda_i F_\nu^S$ is the source spectral energy distribution (the IRAS LRS) and $\alpha \cdot \lambda_i F_\nu^M$ the (renormalized) model, rebinned on the LRS wavelength grid, on which the summation index i runs. The χ^2 variable of each source-model pair was then defined as:

$$\chi^2 = \frac{1}{N-2} \sum_{i=1}^{N} \frac{\left[\lambda_i F_\nu^S\left(\lambda_i\right) - \alpha \cdot \lambda_i F_\nu^M\left(\lambda_i\right)\right]^2}{\sigma_S^2\left(\lambda_i\right) + \sigma_M^2\left(\lambda_i\right)} \tag{4.2}$$

The error σ_S of the IRAS LRS was derived by subtracting the LRS with a smoothed version of themselves, while the error σ_M was estimated as the difference between the two closest models in the parameter space. The χ^2 variable was finally divided by the number of degrees of freedom $N-2$, where $N = 80$ is the number of wavelengths, and 2 are the fitting parameters measured in the fit (τ_V and T_1). Each source was then assigned to its best fit model, providing the minimum value of the χ^2 variable.

As a consistency test for our fitting procedure, we have simulated a set of LRS spectra with known T_1 and τ_V, covering the whole model parameter space, by introducing gaussian noise to our DUSTY model grid. The synthetic spectra were then fitted by using the same original models, without noise. The results are shown in figure 4.10 for $S/N = 10$ and $S/N = 5$ (the first case is the typical one for our sources, and the second corresponds to the most noisy sources in the sample). Each circle in the plots represent a

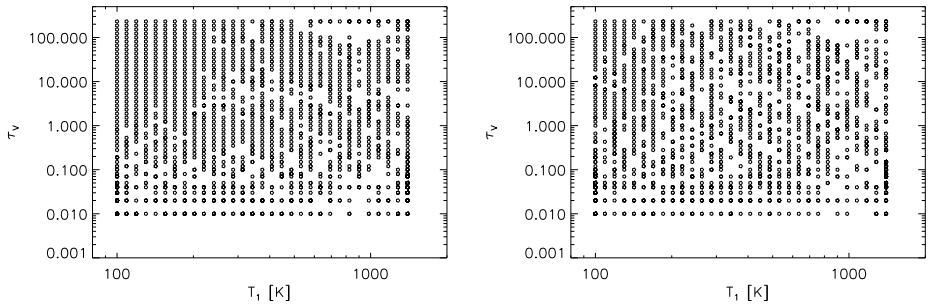

FIG. 4.10.— Test diagram of χ^2 fitting procedure. Artificial gaussian noise have been added to the full grid of models and to the resulting spectra. This produced "noisyfied" spectra, with $S/N = 10$ (left) and 5 (right), which have been fitted using the unmodified grid. Each circle represents one point of the model grid for which the correspondent "noisyfied" model have been successfully fitted. Empty spaces in the regular grid pattern correspond to models not correctly fitted, as a consequence of the added noise.

point in the model grid; missing points are "noisyfied" models which have not been fitted correctly by our procedure.

The figure shows that increasing noise can reduce the effectiveness of our procedure, but within the limits of our sample is not likely to introduce biases in the fit results. The missing points in the grid are distributed uniformly, at least in the regions where the physical parameters of KH sources are expected to fall. Sources with $\tau_V \lesssim 0.02$ are likely to have their optical depth overestimated, due to constraints in the numerical accuracy of the models, which for very low τ_V are practically indistinguishable. The distribution of the incorrectly identified models in T_1 is completely uniform, validating our procedure for fitting this parameter.

4.3.3 Fit results

The quality of our fits is estimated by the value of the best χ^2 variable. As shown in figure 4.11, best fit models with $\chi^2 \lesssim 3$ are in general able to reproduce the source LRS with great accuracy, matching the position of the two silicate features (at 9.8 and 18 μm), their relative height and width, and the slope of the continuum emission. Fits with $3 \lesssim \chi^2 \lesssim 5$, are still good, even though some peculiarity of the silicate feature are not exactly reproduced. The continuum slope, however, is still well modeled, and the small discrepancies are in most cases due to the presence of secondary features, or the unusual width of the source LRS silicate feature, in the 13–14 μm

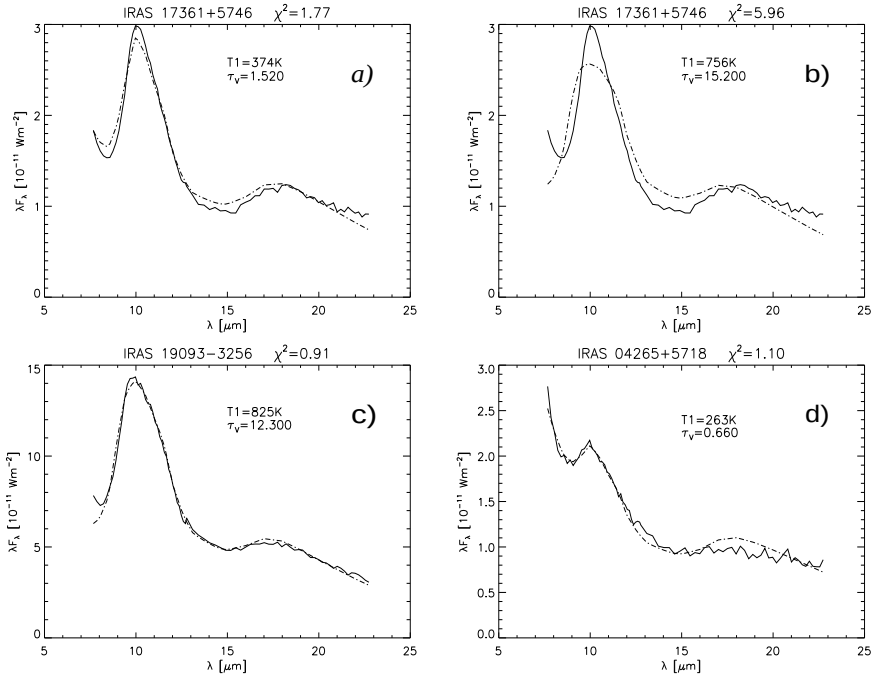

FIG. 4.11.— IRAS Low Resolution Spectra of Mira and NM sources (solid line) with best fit models (dashed dotted line). In panel *a* the SRb star TY Dra is fitted with a cold dust model ($T_1 \simeq 370$ K), resulting in a very small χ^2. If the dust temperature is limited to the range 640–1400 K (as in the "hot dust" models), the fit is unable to reproduce the source spectral energy distribution (panel *b*). Panel *c* and *d* shows good quality fits of a Miras with relatively hot dust ($T_1 \simeq 825$ K) and a SRs with very low inner shell temperature ($T_1 \simeq 270$ K).

range, which cannot be fitted with the Ossenkopf et al. (1992) opacity. A better fit of these models probably requires a larger set of opacities, allowing variations in the dust composition. Models with $\chi^2 \gtrsim 5$, on the other hand, show more serious problems, as the wrong fit of dust continuum emission, or failure in the fitting routine convergence, due to insufficient S/N in the source LRS. The best fit parameters obtained for these sources are less reliable, since a better fitting may require radically different opacities, or changes in the envelope geometry, such as the presence of multiple dust shells.

The statistics of the best fit χ^2 for our KH sources is shown in table 4.3. The left side of the table reports the number of sources having χ^2 larger than 3, 5 and 10 in the Miras, NMs, SRa and period selected SRs, fitted

Table 4.3 Sources which cannot be fitted with χ^2 better than 3, 5 and 10.

	all models			hot models		
Sample	$\chi^2 \gtrsim 3$	$\chi^2 \gtrsim 5$	$\chi^2 \gtrsim 10$	$\chi^2 \gtrsim 3$	$\chi^2 \gtrsim 5$	$\chi^2 \gtrsim 10$
Mira	35%	19%	3%	42%	31%	12%
NM	18%	6%	1%	54%	27%	22%
SRa	21%	4%	2%	33%	12%	4%
SR ($P<100^d$)	18%	5%	0%	67%	42%	21%
SR ($P\gtrsim100^d$)	21%	7%	2%	48%	18%	6%

with the full grid of models. The right side present the same statistics, but with the use of the "hot dust" family of models (models with $T_1 \gtrsim 640$ K). Notice that all NM sources shows a significant improvement in the quality of their fits when "cold dust" models ($T_1 \lesssim 640$ K) are allowed (compare, e.g. panels *a* and *b* of figure 4.11), while Miras can be equally well fitted using "hot dust" models alone. This is a further evidence that the class of NM is more likely to show colder envelopes than the average Mira source.

4.4 Correlation between mass loss rate and shell temperature

The statistical distribution of the best fit parameters for our KH sample can be analyzed to test the separation between Miras and NMs suggested by the different colors and silicate feature position.

This statistical analysis is limited to sources with χ^2 better than 10, in order to prevent unreliable fits to bias our conclusions. This restriction is aimed to exclude the sources in which the continuum emission is not exactly reproduced by the model, and thus the fitting procedure is suspected to have converged on mistaken best fit parameters. The excluded sources are 19% of the Miras, and 6% of the NMs.

This precautional measure, however, does not seem to affect the statistical validity of our results: similar tests performed on the whole sample yielded the same conclusions, within the approximations of our technique.

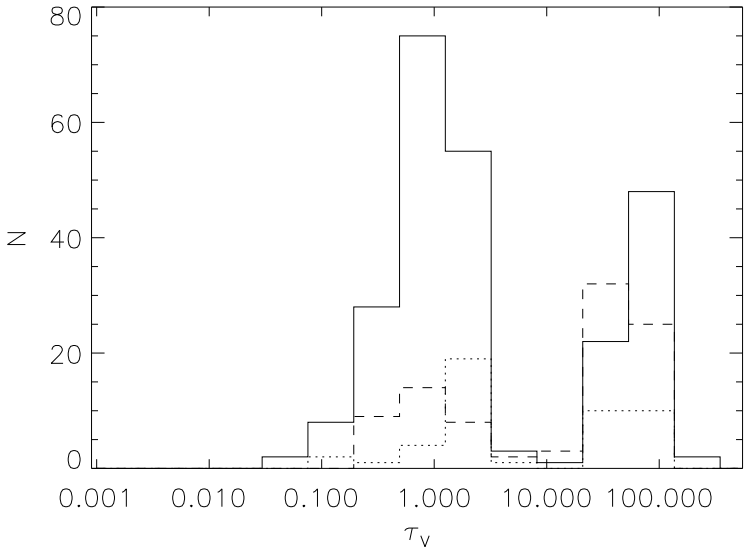

FIG. 4.12.— Distribution of the best fit optical depth τ_V for Miras (dashed line), NMs (solid line) and SRa (dotted line).

4.4.1 Distribution of envelope optical depths

Figure 4.12 shows the statistical distribution of the best fit optical depth for our KH sources. The histogram appears to be bi-modal, with a double-peak distribution centered at $\tau_V \sim 1$ and $\tau_V \sim 25$ respectively. NMs appears to be distributed mainly in the low τ_V bin, while Miras, although present in both categories, are mainly concentrated in the high optical depth bins. SRa appears to be equally distributed in the two categories, with a prevalence for low optical depths.

This diagram reflects a well known characteristic of LPVs: Miras in general possess higher optical depths than non-Miras, which on the contrary are in general brighter optically. From the analysis of our sample it is difficult to decide if the separation between the low and high τ_V distribution is statistically significant: larger statistics and a more accurate fit with better opacities is probably necessary to validate this result. The different average optical depth of the two main classes (Mira and NM), is however large enough to be confirmed by the statistical tests reported in table 4.4.

Note that the Student's t-test in table 4.4 underestimates the difference between the various populations, since it analyses the mean value assuming

TABLE 4.4 DISTRIBUTION OF BEST FIT τ_V FOR KH SOURCES.

Sample	Median	Mean	σ	N sources ($\chi^2 \lesssim 5$)
Mira	23.1	25.4	21.8	81 (81%)
NM	1.2	16.6	25.9	232 (94%)
SRa	2.3	20.9	25.1	46 (96%)
SR ($P < 100^d$)	0.8	10.5	25.8	54 (95%)
SR ($P \gtrsim 100^d$)	1.5	20.2	26.2	121 (93%)

Significance of statistical tests

Sample	F-test	t-test	Result at 0.01 significance[a]
Mira vs. NM	0.08	$7 \cdot 10^{-3}$	Same σ and different mean
SRa vs. Mira	0.28	0.30	Same σ and mean
SRa vs. NM	0.83	0.29	Same σ and mean
SR $P<100^d$ vs. $P\gtrsim100^d$	0.92	0.02	Same σ and mean

[a] Samples have different σ if the variance F-test returns a significance of 0.01 or smaller, and different mean values if Student's t-test returns a significance of 0.01 or smaller.

a gaussian distribution. This is of course not valid for the bimodal distributions shown in figure 4.12. A much better comparison between the different subsamples is given by the median values of the best fit τ_V, which are closer to the modal value for each sample. In this case, SRa appears to be more similar to NMs than to Miras, even though the Student's t-test cannot decide on the basis of the mean value. This confirms that our SRa does not have a large contamination of Miras. The two subclasses of NMs appears to have similar optical depths, even though short period NMs tends to have lower τ_V.

4.4.2 Distribution of inner shell temperatures

If the segregation between Miras and NMs is related to an intrinsic difference in the underlying mass loss mechanism, a correlation between the best fit τ_V and T_1 should be expected. This is shown in figure 4.13, where the KH sources appear distributed in a strip crossing the diagram. Even though

both classes of sources are present along the whole sequence, Miras tend to aggregate at the top of the strip, with higher optical depths and T_1. NMs, on the contrary, have in general lower T_1 and τ_V. A discontinuity in the distribution of the sources for $T_1 \simeq 500$ K, suggests to divide the diagram in 4 separate regions, labeled counter-clockwise from I to IV, with most of the sources in quadrant I and III only. A quantitative distribution of the various subclasses in the four quadrants is given in table 4.5.

The sequence observed in figure 4.13 can be explained by assuming that low T_1 are the product of envelope expansion, after the interruption of the mass loss rate. At the end of an intense dust production phase, an envelope starting at the inner radius R_c (dust condensation radius) will have a "steady state" radial profile $n_d(r) \simeq n_d(R_c) \cdot (R_c/r)^2$. If the dust production stops, the envelope would detach, expanding at a radius $R_1 = R_c + v_e t$, where v_e is the expansion velocity and t the time since the envelope detachment. From equations 2.29 and 2.65, the optical depth of the detached envelopes can be written as:

$$\tau_V \simeq \pi a^2 \cdot Q_V \cdot n_d(R_c) \, \frac{R_c^2}{R_1} \sim \tau_V(0) \, \left(\frac{1}{1 + \frac{v_e t}{R_c}} \right) \tag{4.3}$$

where $\tau_V(0)$ is the optical depth that the envelope built-up just before detaching from the stellar atmosphere. Since the stellar flux scales as r^{-2}, and the cooling radiative flux of the grains as T_d^4, the equilibrium temperature of the dust at the inner envelope edge goes as $R_1^{-1/2}$. Taking into account radiative transfer effects, one has from equation 2.38:

$$T_1 \simeq T_c \left(\frac{R_c}{R_1} \right)^n \simeq T_c \left(\frac{1}{1 + \frac{v_e t}{R_c}} \right)^n \tag{4.4}$$

with $n = 2/(4 + \beta)$, and $\beta \sim 1$–2 for silicate and amorphous carbon dust. Equations 4.3 and 4.4 describe a linear relation on the logarithmic τ_V - T_1 plane, parametrized on the time t after the envelope detaches:

$$\log \tau_V \simeq \log \left[\tau_V(0) \right] + k \, \log \left[\frac{T_1}{T_c} \right] \tag{4.5}$$

where $k \simeq (4 + \beta)/2 \sim 2.5$–$3.0$. Linear interpolation of the sources in figure 4.13 gives a very similar result, with a best fit regression line, for all sources, that is approximately:

$$\log \tau_V \simeq \frac{3}{2} + \frac{5}{2} \cdot \log \left(\frac{T_1}{1000\mathrm{K}} \right) \tag{4.6}$$

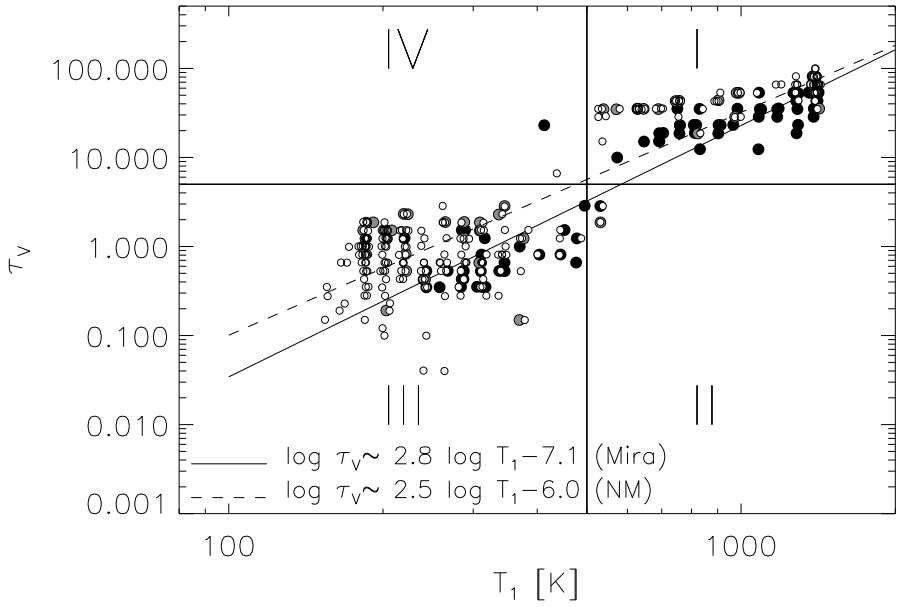

FIG. 4.13.— Model τ_V vs. T_1 for Miras (filled circle), non-Miras (empty circles) and SRa (grey symbols). A small random offset (less than 1/3 of the parameter grid step) has been added to each T_1 and τ_V, in order to separate the symbols associated to sources with identical best fit parameters, which would otherwise appear as a single point on the diagram. The plot is divided in four regions, according to the source segregation; the counts in the four quadrants are given in table 4.5.Regression lines for Miras and NMs are plotted.

TABLE 4.5 KH SOURCES DISTRIBUTION IN τ_V VS. T_1 DIAGRAM.

Sample	I	II	III	IV
Mira	59	1	32	1
NM	72	2	169	1
SRa	20	1	26	0

This confirms that the distribution of the sources in the T_1 / τ_V space are well represented by the hypothesis of detached shells after a phase of enhanced mass loss.

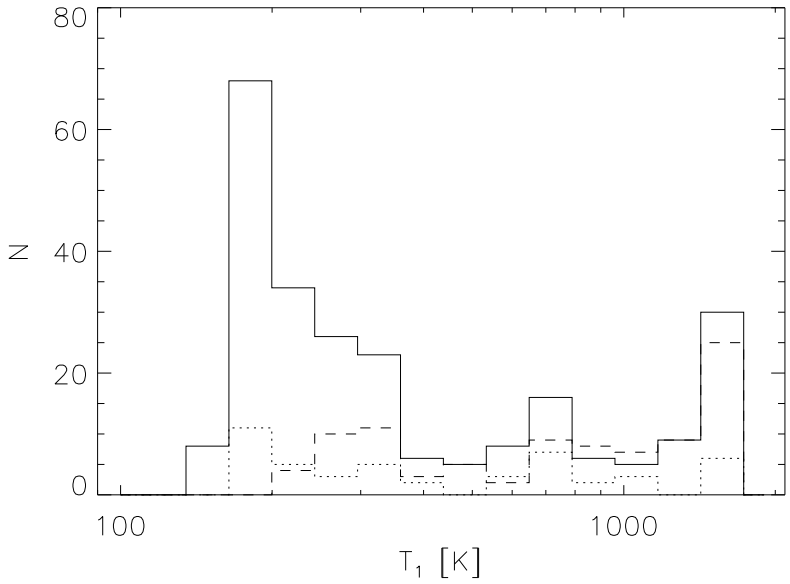

FIG. 4.14.— Histogram of T_1 distribution for KH Miras (dashed line), NM (solid line) and SRa (dotted line).

The details of the source distribution on the plot, and in particular the steep discontinuity in $\log \tau_V(0)$ shown by all sources around $T_1 \sim 500$ K may be due to a sudden drop in the dust production and growing processes when the temperature of the inner shell drops, due to its expansion, below a critical value, making inefficient the dust accumulation mechanisms.

The hypothesis of detached shells can also predict the distribution of the sources $\mathrm{d}N/\mathrm{d}T_1$ in each temperature bin:

$$\frac{\mathrm{d}N}{\mathrm{d}T_1} = \frac{\mathrm{d}N}{\mathrm{d}t} \cdot \frac{\mathrm{d}t}{\mathrm{d}T_1} \tag{4.7}$$

where $\mathrm{d}N/\mathrm{d}t$ is the distribution of sources as a function of the time t in which the envelope detached. Assuming a constant expansion rate, $\mathrm{d}N/\mathrm{d}t \sim const$ and $\mathrm{d}T_1/\mathrm{d}t \propto \mathrm{d}T_1/\mathrm{d}R_1 \simeq R_1^{-n-1} \propto T_1^{n+1/n} \simeq T_1^3$ (using equation 4.4), and thus:

$$\frac{\mathrm{d}N}{\mathrm{d}\log T_1} \propto T_1 \cdot \frac{\mathrm{d}t}{\mathrm{d}T_1} \simeq T_1^{-2} \tag{4.8}$$

TABLE 4.6 DISTRIBUTION OF BEST FIT T_1 FOR KH SOURCES.

Sample	Median [K]	Mean [K]	σ [K]	N sources ($\chi^2 \lesssim 5$)
Mira	830	870	430	81 (81%)
NM	290	490	430	232 (94%)
SRa	370	560	410	46 (96%)
SR ($P < 100^d$)	200	360	350	54 (95%)
SR ($P \gtrsim 100^d$)	310	480	450	121 (93%)

Significance of statistical tests

Sample	F-test	t-test	Result at 0.01 significance[a]
Mira vs. NM	0.86	$9 \cdot 10^{-11}$	Same σ and different mean
SRa vs. Mira	0.72	$1 \cdot 10^{-4}$	Same σ and different mean
SRa vs. NM	0.78	0.35	Same σ and mean
SR $P<100^d$ vs. $P\gtrsim100^d$	0.04	$2 \cdot 10^{-3}$	Same σ and different mean

[a] Samples have different σ if the variance F-test returns a significance of 0.01 or smaller, and different mean values if Student's t-test returns a significance of 0.01 or smaller.

The histogram shown in figure 4.14 agrees with this dependence for the sources on NM class. For example, there are about 6 times more sources in the $T_1 = 200$ K bin than in the $T_1 = 500$ K bin, in nice agreement with the prediction in equation 4.8.

The distribution of NMs is sharply truncated for $T_1 \sim 200$ K, even though our model grid continues as low as $T_1 = 100$ K. This results suggests that when the NMs envelope has expanded to a distance at which the equilibrium temperature is $\sim$ 150–200 K, a new hot shell is formed, bright enough to dominate the LRS spectrum from which the fit is made.

Note that the same lower value of T_1 was estimated by superposing the model tracks on the "silicate" diagram in figure 4.9. This lower limit in the dust inner shell temperature of all sources can be used to derive the maximum time in which the mass loss is suspended in NMs sources, by using the radial dependence $T_d(r)$ in equation 4.4. Since the distance R_c at which the silicate dust can form ($T_c \simeq 1500$ K) is, for a typical O-rich AGB with $T_{eff} \simeq 200$ K, of the order of a few stellar radii ($R_c \simeq 5$–$8 \cdot 10^{13}$ cm),

one can write:

$$R_1 \sim 5 - 8 \cdot 10^{13}\,\mathrm{cm} \left(\frac{1500\mathrm{K}}{T_1}\right)^2 \tag{4.9}$$

being $R_s \sim 1$ A.U. the average stellar radius in the AGB phase. A dust shell with $T_1 \simeq 200$ K should thus be located at a distance $R_1 \simeq 0.9$–$1.7 \cdot 10^{16}$ cm. Assuming an expansion speed about 15 km/s, the required time to produce a detached shell at such distance is then 100–200 yr. Note that the estimated time scale is too long to compare with the Mira/SR pulsational period, and too short with respect to the interpulse time in the TP-AGB phase. It is however consistent with the timescales observed by Hashimoto et al. (1998); Sahai et al. (1998); Mauron & Huggins (1999), and by the independent estimate made in section 3.3.5 (see also Marengo et al., 1999).

The timescale of the high mass loss duration phase, in which the dust envelopes are created, can also be estimated by counting the fraction of NMs in the high temperature bins (e.g. $T_1 \gtrsim 500$ K). Since this fraction is about 30%, the phase of intense dust production should last no more than 30–60 yr, assuming 100-200 yr as the total period of the mass loss cycle.

Miras, on the contrary, show a flat distribution, truncated at a much higher T_1. This is an evidence that Mira sources have a higher dust production efficiency, which prevents the complete detachement of their circumstellar envelopes, and their cooling to very low temperatures.

The parameters of the T_1 distribution for the various subsamples are written in table 4.6. They confirm the separation between Miras and NMs and the homogeneity of SRa with the global NM class. The two subclasses of SRs with long and short pulsational period, however, does show a different mean value, with short period SRs having colder dust than the long period ones. This difference, however, has low statistical significance, and can be due to statistical fluctuations in our sample.

4.4.3 Distribution of mass loss rates

From the best fit parameters of each source, it is possible to estimate the mass loss rate. By integrating the differential optical depth along the path as in equation 4.3, with a "steady mass loss" radial density profile $n_d(r) \simeq n_d(R_1) \cdot (R_1/r)^2$, one obtains:

$$\tau_V \simeq \pi a^2 \cdot Q_V \cdot n_d(R_1) R_1 \tag{4.10}$$

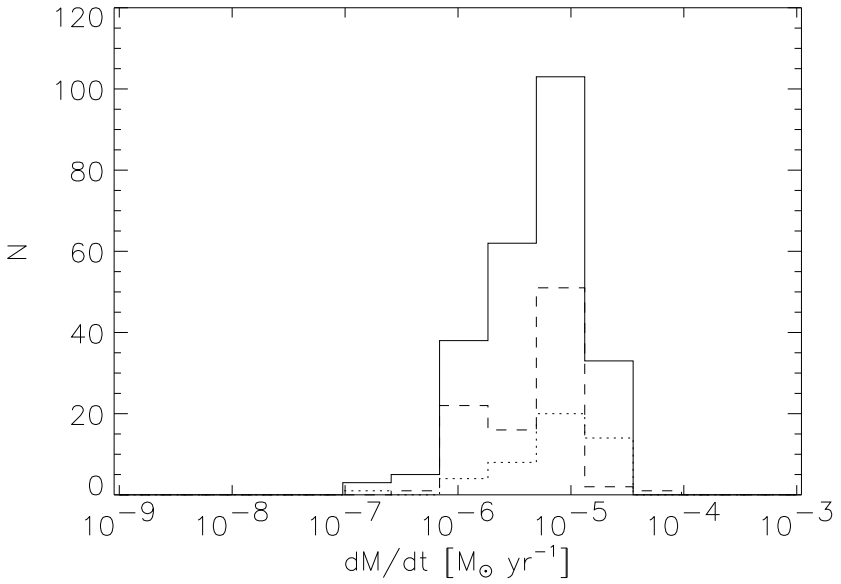

FIG. 4.15.— Distribution of best fit mass loss rate $\dot{M}$ for Miras (dashed line), NMs (solid line) and SRa (dotted line).

where a is the dust average grain radius and Q_V the opacity at optical wavelength. For a spherically symmetric dust envelope with constant expansion velocity v_e, the mass loss rate is:

$$\dot{M} \simeq 4\pi r^2 \cdot v_e \cdot \mu_d \rho_r \tag{4.11}$$

where μ_d is the dust to gas mass loss ratio and $\rho_r \simeq 4/3\pi a^3 \cdot \rho_d \cdot n_d(r)$ the mass density distribution of the circumstellar shell, made of individual dust grains having mass density ρ_d. Combining equation 4.10 with equation 4.11 one has:

$$\dot{M} \simeq \frac{16\pi a}{3} \cdot \frac{\mu_d \rho_d \cdot v_e}{Q_V} \cdot \tau_V \cdot R_1 \tag{4.12}$$

For the sources in our KH sample, one can assume $\rho_d \simeq 3.9$ g cm^{-3} as in terrestrial silicates, $a \simeq 0.1$ μm, $Q_V \simeq 1$, $v_e \simeq 15$ km/s and $\mu_d \simeq 100$. Using equation 4.9, one finally obtains the following approximation for the mass loss rates, as a function of the two fitting parameters τ_V and T_1 alone:

TABLE 4.7 DISTRIBUTION OF BEST FIT $\log_{10}(\dot{M}/1\mathrm{M}_{\odot}\mathrm{yr}^{-1})$ FOR KH SOURCES.

Sample	Median	Mean	σ	N sources ($\chi^2 \lesssim 5$)
Mira	-5.3	-5.4	0.3	81 (81%)
NM	-5.4	-5.4	0.4	232 (94%)
SRa	-5.1	-5.2	0.4	46 (96%)
SR ($P < 100^d$)	-5.5	-5.5	0.4	54 (95%)
SR ($P \gtrsim 100^d$)	-5.3	-5.3	0.4	121 (93%)

Significance of statistical tests

Sample	F-test	t-test	Result at 0.01 significance[a]
Mira vs. NM	0.14	0.46	Same σ and mean
SRa vs. Mira	0.14	$2 \cdot 10^{-3}$	Same σ and different mean
SRa vs. NM	0.66	$6 \cdot 10^{-3}$	Same σ and different mean
SR P<100^d vs. $P\gtrsim$100^d	0.59	$8 \cdot 10^{-3}$	Same σ and different mean

[a] Samples have different σ if the variance F-test returns a significance of 0.01 or smaller, and different mean values if Student's t-test returns a significance of 0.01 or smaller.

$$\dot{M} \simeq 0.1 \cdot \tau_V \left(\frac{1\mathrm{K}}{T_1}\right)^2 \tag{4.13}$$

Note that this quantity represent the mass loss rate at the time in which the dust shell was produced. In the case of detached envelopes, this is not the current mass loss rate, which may be significantly lower.

The histogram with the distribution of $\dot{M}$ is shown in figure 4.15. All classes reveal a similar distribution centered around $\log_{10}(\dot{M}/1\mathrm{M}_{\odot}\mathrm{yr}^{-1}) \simeq -5.3$, and a similar spread, with $\dot{M}$ in the interval 10^{-7}–$5 \cdot 10^{-5}$ $\mathrm{M}_{\odot}$ yr^{-1}. This result implies that Miras and NMs does have a similar total mass loss rate, at least during the high dust production phase which resulted in the creation of the dust shell.

Table 4.7 reports the statistics of the distribution. The similarity between Mira and NM mass loss is confirmed, even though a separation of SRa from the other classes, and between the two classes of SRs with different pulsational period, is suggested. The significance of the separation

is however very low, and can be attributed to statistical fluctuations in our sample, or to the high uncertainties in the quantities assumed to derive equation 4.13 (and in particular the dust to gas mass loss ratio and the average grain size).

4.5 Conclusions

In this analysis we have investigated the connections between mass loss and variability for a sample of AGB LPV of Mira, SR and Irregular type, from the point of view of the mid-IR emission of their dusty circumstellar envelopes.

We found the continuum excess color in the 12.5 and 18.0 μm bands able to differentiate between sources of Mira and NM type. NMs showed a higher [12.5]-[18.0] color, which we interpreted as an indication of missing hot dust in the circumstellar envelope of these sources.

We then compared the position of 10 μm silicate feature in the LRS spectrum of Mira and NM sources, confirming the shift of ~ 0.2 μm already found by other authors. Even though this result may be taken as an evidence for mineralogical variability in the composition of oxidic dust in the two class of sources, we have pointed out how radiative transfer may mimic the same effect. If this is the case, the shift observed in the LRS of NMs can be another consequence of colder dust in their envelopes.

We then applied radiative transfer modeling to all sources in the sample, in order to derive their optical depth and temperature at the inner shell boundary by fitting their individual Low Resolution Spectra. Again we found a statistically significant difference between the temperature of NM and Mira circumstellar envelopes.

About 70% of all NMs in our sample show a τ_V vs. T_1 relation that is appropriate for detached envelopes, expanding freely at the AGB wind speed. For these sources, the inner boundary shell temperature is much lower than the dust condensation one, but never less than 150–200 K. This minimum temperature can be interpreted as a maximum limit of 100-200 yr in the period of time in which the envelopes are allowed to detach, before being replaced by newly formed hot structures. The remaining part of the NMs are instead characterized by much hotter envelopes with an estimated T_1 in the dust condensation and growth range ($Tc \sim$ 600–1400 K), in which the envelope is not complete detached. The frequency of these sources ($\sim$30%) suggests that the duration of the high mass loss phase in NMs is of the order of 30–60 yr. The two regimes are linked by an intermediate domain, in

which $T_1 \sim 500$ K, where the optical depth of the envelope suddenly drops by one order of magnitude.

The proportion between "hot" and "cold" envelopes in the Mira class is reversed with respect to NMs, with 70% of Miras having $T_1 \gtrsim 500$ K. This dependence shows that fully detached shells are probably not common in the Mira class. The 1 magnitude drop in the total optical depth of the envelopes around $T_1 \sim 500$ K, is confirmed for this class of sources, and can thus be related to some basic property of the silicate dust condensation processes.

We did not find any significant difference in the total mass loss rates of Miras and NMs, even though the frequent occurrence of detached shells in NMs suggests the existence of intermittent phases in which the dust production is suspended for these sources.

All our statistical tests confirm that our subsample of SRa is coherent with the full sample of NMs (SRa, SRb and Irregulars) in our selection of KH sources. We also did not find any significant difference between SRs with long and short period pulsations, that can be associated with different phases in the AGB evolution.

As suggested by Ivezić & Knapp (1998), the absence of hot dust in NMs can be interpreted as a recent decrease ($\sim 10^2$ yr) in their mass loss rates. In the same paper were also found evidences for mass loss to resume on similar timescales, implying that AGB stars may oscillate between the Mira and NM phase, as proposed by Kerschbaum & Hron (1996). This idea is however discarded in a recent paper by Lebtzer & Hron (1999), in which the abundance of ^{99}Tc in a large sample of SRs was compared with the analogous quantity in Miras. Since the Tc abundance is characterized by a quick increase during the first thermal pulse, after which it stays basically constant (Busso et al., 1992), a similar fraction of Tc-rich stars should be found in the Mira and SR samples. However, this is not the case, making it unlikely that TP-AGB variables oscillates between the two classes of pulsators.

Our analysis confirms the occurrence of shell detachment in NM variables, but suggests a different explanation. The discordant behavior of mass loss between Miras and NMs may be due to a different efficiency of oxidic dust formation in the two cases. This may be related to the characteristic pulsational mode of the two classes of variables.

Many separate evidences points toward the idea that SR variables pulsate as a combination of several overtones, while Miras are high amplitude pulsators (Wood et al.,, 1999), even though this subject is quite controversial (see e.g.Feast 1999, proceedings of the same I.A.U. conference). If this is the case, it is likely for Mira variables to have a greater efficiency in lev-

itating their extended atmosphere to regions where the dust condensation is possible (see discussion of Icke et al. 1992 models in Sahai et al. 1998). As a consequence, Miras extended atmospheres would be able to support a continuous mass loss rate by providing enough molecules in the right density and temperature range for dust condensation and growth. NMs, on the contrary, would need several pulsation cycles to reach the critical density for dust formation to start. The increasing opacity resulting from dust nucleation would then trigger an outburst of dust production, lasting until the dust building elements are depleted, after which the envelope detaches. In this case, the active phase in which the mass loss is active in NM variables should be of the order of 30%, of the total cycle, according to the ratio of NMs which do not show a detached shell.

This dynamical mechanism has been partially reproduced in time dependent wind models (Winters, 1998), but the observed timescales (5–10 yr) are still too short to explain the observed shells. Based on our analysis, we cannot favor any particular mechanism for the occurrence of interrupted mass loss in NM sources. We feel, however, that dynamical models trying to reproduce the mass loss of AGB pulsators should take into account this link between the efficiency of dust production and the pulsational type, and the presence of detached dust shells found by analyzing the relations between τ_V and T_1 in the two classes of sources.